Wall model based on neural networks for LES of turbulent flows over periodic hills

Zhideng Zhou, Guowei He, and Xiaolei Yang [*]

State Key Laboratory of Nonlinear Mechanics, Institute of Mechanics, Chinese Academy of Sciences, Beijing 100190, China
and School of Engineering Sciences, University of Chinese Academy of Sciences, Beijing 100049, China

In this work, a data-driven wall model for turbulent flows over periodic hills is developed using the feedforward neural network (FNN) and data from wall-resolved large-eddy simulation (WRLES). To develop a wall model applicable to different flow regimes, the flow data in the near-wall region at all streamwise locations are grouped together as the training data set. In the developed FNN wall models, we employ the wall-normal distance, near-wall velocities, and pressure gradients as input features and the wall shear stresses as output labels, respectively. *A priori* tests on the prediction accuracy and generalization capacity of the trained FNN wall model are carried out by comparing the predicted wall shear stresses with the WRLES data from the same cases for model training and the cases with different Reynolds numbers and hill geometries. For the instantaneous wall shear stress, the FNN predictions show an overall good agreement with the WRLES data with some discrepancies observed at locations near the crest of the hill. The correlation coefficients between the FNN predictions and WRLES predictions are larger than 0.7 at most streamwise locations. For the mean wall shear stress, the FNN predictions agree very well with WRLES data. *A posteriori* test is also carried out. A good performance is observed for the turbulent channel flow case. Discrepancies between the predictions from the wall-modeled LES and the WRLES are observed for the periodic hill case.

I. INTRODUCTION

Separation and reattachment in turbulent flows over curved surfaces exist in numerous environmental and industrial processes, e.g., underwater vehicle, fuselages at high incidence, curved ducts, and stalled wings and turbine blades. Such flows are difficult to predict accurately using the Reynolds-averaged Navier-Stokes (RANS) method due to nonequilibrium spatial and temporal fluctuations, although it is widely used in engineering applications. On the other hand, large-eddy simulations, which directly solve energetic turbulence scales, model the subgrid scales, and are significantly less computational expensive than direct numerical simulation (DNS) [1–3], provide a feasible way for simulating complex turbulent flows with separation and reattachment at a reasonable cost. However, it is still not applicable to employ wall-resolved large-eddy simulation (WRLES) in the design and optimization of high Reynolds number turbulent flow problems in real life because of the extremely high resolution needed to resolve the viscous scale near the wall [2,4]. To reduce the computational cost of WRLES, wall models are employed in the literature [5,6] to avoid the need to resolve the small-scale turbulence in the near-wall region, providing a feasible way for LES of wall-bounded flows at high Reynolds number. However, most existing

---

*Corresponding author: xyang@imech.ac.cn

054610-1

wall models [7,8] based on equilibrium hypothesis are incapable of predicting flow separations and reattachments. The development of machine learning methods [9,10] and the availability of high-resolution data from experiments and high-fidelity simulations provide another possible approach for developing advanced wall models for complex turbulent flows. As the first step, in this work we develop the wall models based on neural networks for turbulent flows over periodic hills.

We first briefly review different wall models developed in the literature. In wall-modeled LES (WMLES), the turbulent flow near the wall is described by a wall-layer model with its influence on the outer flow represented by appropriate boundary conditions. The wall-stress model is the most widely used one in the literature, in which the wall shear stress is computed and provided as boundary conditions for outer flow simulations. Different models have been developed in the literature for computing wall shear stress, which include the equilibrium-stress model and zonal model (also dubbed as the two-layer model) [8]. The algebraic equilibrium-stress models assume a constant-stress layer near the wall [11] and calculate the wall shear stress using the law of the wall of deterministic form [7]. The algebraic model has the advantage of low computational cost, but it cannot accurately predict the wall shear stress in nonequilibrium flows, for which the equilibrium-stress hypothesis is no longer valid. The zonal model, on the other hand, solves the thin-boundary-layer equation (TBLE) on an embedded grid between the first grid point and the wall. Wang and Moin [12] systematically studied the efficacy of zonal models and found that the instantaneous wall shear stress cannot be accurately predicted when the nonequilibrium terms are ignored or the pressure gradient term is only considered. Later, the dynamic zonal models were proposed, which adjust mixing-length eddy viscosity in TBLE, and were shown to be able to predict low-order turbulence statistics [13,14]. Park [15] applied two standard zonal models, a nonequilibrium and an equilibrium one, to predict the flow over a wall-mounted hump, and found that the nonequilibrium model gives better predictions of the mean velocity and force on the wall in the region with flow separation and reattachment. The integral wall model was also developed in the literature [16], which introduces an additional linear term into the equilibrium logarithmic velocity profile and accounts for near-wall nonequilibrium effects by solving the vertically integrated momentum equation. However, this model has only been tested in applications in which the nonequilibrium effects is insignificant. Lozano-Durán *et al.* [17] investigated the performance of three different wall models, an equilibrium one [18] and two nonequilibrium ones [14,16], for a nonequilibrium three-dimensional channel flow. They found that increasing the degree of modeling complexity reduces the errors in WMLES of the considered flow. Besides the wall-stress type models, the virtual-wall model was also developed by aligning the slip velocity in the integrated TBLE on the virtual wall [19,20]. It has been demonstrated to be capable of capturing the quantitative features of a separation-reattachment turbulent boundary-layer flow at low to moderately large Reynolds numbers. However, the identification of virtual wall in a virtual-wall model is challenging for flows with complex geometries. Recently, the dynamic slip wall model was developed [21,22] to model the wall shear stress from the derivation of the LES equations using a differential filter, but its accuracy is sensitive to the subgrid-scale (SGS) models and numerical methods. The conventional wall models have been applied to different kinds of flows [8,23–25], but they still cannot accurately predict the flow separation and reattachment. Advanced wall models accounting for such nonequilibrium effects has yet to be developed.

Thanks to the exponential growth in computing power, the increasing amount of high-fidelity data provides a possibility to develop data-driven wall models to resolve the above issues. The data-based approaches, particularly the machine learning (ML) method, have been applied to various turbulence problems, e.g., the development of turbulence models [26,27], temporal prediction of turbulence [28,29], and reconstruction of the turbulent flow fields [30,31]. For the applications of the ML method in developing RANS models, Ling *et al.* [26] presented a deep neural network for RANS turbulence modeling on an invariant tensor basis [32]. Xiao and coworkers [33,34] developed a physics-informed ML framework to learn Reynolds stress discrepancies between RANS and DNS. Duraisamy *et al.* [9] reviewed in detail the recent developments of RANS turbulence models based

on ML. As for LES models, the ML has been applied to model the SGS stresses in different flows including the turbulent channel flows [35], two-dimensional decaying turbulence [36], and isotropic turbulence [27] and to model the SGS scalar flux [37]. For the wall-bounded turbulent flows, the ML was also employed to develop wall models [38], which is the major concern of this work. Recently, Yang *et al.* [39] developed a wall-stress model for LES of turbulent channel flow using DNS data and physics-informed neural networks. They found that the trained wall model outperforms the conventional equilibrium wall model in simulating the three-dimensional boundary-layer flow, which can be considered to have a nonequilibrium effect. A similar neural network was then applied to spanwise rotating turbulent channel flows with a discussion on the performance of physics-based and data-based approaches [40]. However, to the best of our knowledge, the nonequilibrium effects, e.g., pressure gradients, curvature, and separation, which are important for complex turbulent flows in engineering applications, have not been fully taken into account in the existing data-driven wall model and need to be systematically investigated.

Characteristics of complex wall-bounded turbulent flows depends on the geometry of the boundary and the corresponding boundary conditions. Development of a data-driven nonequilibrium wall model applicable to different types of turbulent flows requires a significant amount of data of different flows, which is beyond the scope of this work, will be carried out in our future work. An attempt to develop such a data-driven wall model framework has been carried out by Lozano-Durán and Bae [41], which includes a predictor of wall models trained using different data and a classifier giving a confidence value for different types of flows. The flow over periodic hills, in which the flow is featured by separation from a curved surface, recirculation, reattachment, and strong pressure gradient, is an ideal generic test case for developing statistical closures for separated flow [42]. Different wall models have been applied to simulate the flow over periodic hills. For instance, Temmerman *et al.* [43] applied the equilibrium wall models to simulate the flow over periodic hills and found that the sensitivity of the solution to the SGS model is less than that to grid resolution and wall model. Furthermore, they demonstrated that the WMLES cannot accurately predict the flow separation, reattachment, and related statistics. To simulate the flow over periodic hills, Manhart *et al.* [44] proposed an extended inner scaling for the wall layer of wall-bounded flows under the influence of both wall shear stress and adverse pressure gradient. Duprat *et al.* [45] constructed a different wall model based on the simplified TBLE, which takes into account both the streamwise pressure gradient and the Reynolds stresses effects, and applied it to simulate the flow over periodic hills. It was shown that their proposed model yields good results for predictions of first-order statistics and reproduction of flow separation. To investigate in detail the separation and reattachment process, Breuer *et al.* [46] carried out numerical and wind tunnel experiments of the flow over periodic hills at various Reynolds numbers in the range of 100 to 10 595. Rapp and Manhart [47] experimentally investigated the flow over periodic hills at four Reynolds numbers ranging from 5600 to 37 000. Krank *et al.* [48] carried out DNS of the flow over periodic hills at Reynolds number 10 595, which is the highest fidelity to date. Moreover, Xiao *et al.* [49] constructed benchmark data sets for the flow over periodic hills by performing DNS with varying flow configurations to alleviate the lack of data for training and testing data-driven models.

The objective of this work is to develop a data-driven wall model for the flow over periodic hills using the feedforward neural network (FNN) and WRLES data. The data sets employed for training the model consist of flow field data in the near-wall flow region at all streamwise locations with different flow features. To train the FNN wall model, we employ the wall-normal distance, near-wall velocities, and pressure gradients as input features and the wall shear stresses as output labels, respectively. The trained wall model is evaluated using the data from different snapshots and spanwise slices for both training and testing data sets.

The rest of the paper is organized as follows: In Sec. II, WRLES of the flow over periodic hills is briefly described, which is followed by the procedure for preparing data sets for training and testing FNN models. Then the feedforward neural network is introduced and trained in Sec. III. At last, conclusions from this work are drawn in Sec. V.

II. DATA GENERATION AND PREPARATION

A. Data generation using wall-resolved large-eddy simulation

In this section, we describe the numerical method and the case setup for generating the data employed for developing a data-driven wall model, which can take into account the nonequilibrium effects, e.g., flow separation and reattachment, for turbulent flows over periodic hills.

We employ the VIRTUAL FLOW SIMULATOR (VFS-WIND) [50,51] code for WRLES of turbulent flows over periodic hills. The VFS code has been successfully applied to industrial and environmental turbulent flows [52–59]. In the VFS-WIND code, the governing equations are the three-dimensional unsteady spatially filtered incompressible Navier-Stokes equations in nonorthogonal, generalized curvilinear coordinates shown as follows:

$$J\frac{\partial U^j}{\partial \xi^j} = 0,$$

$$\frac{1}{J}\frac{\partial U^i}{\partial t} = \frac{\xi_l^i}{J}\left(-\frac{\partial}{\partial \xi^j}(U^j u_l) - \frac{1}{\rho}\frac{\partial}{\partial \xi^j}\left(\frac{\xi_l^j p}{J}\right) + \frac{\mu}{\rho}\frac{\partial}{\partial \xi^j}\left(\frac{g^{jk}}{J}\frac{\partial u_l}{\partial \xi^k}\right) - \frac{1}{\rho}\frac{\partial \tau_{lj}}{\partial \xi^j} + f_l\right),$$

(1)

where x_i and ξ^i are the Cartesian and curvilinear coordinates, respectively, $\xi_l^i = \partial \xi^i/\partial x_l$ are the transformation metrics, J is the Jacobian of the geometric transformation, u_i is the ith component of the velocity vector in Cartesian coordinates, $U^i = (\xi_m^i/J)u_m$ is the contravariant volume flux, $g^{jk} = \xi_l^j \xi_l^k$ are the components of the contravariant metric tensor, ρ is the fluid density, μ is the dynamic viscosity, and p is the pressure. In the momentum equation, τ_{ij} represents the anisotropic part of the subgrid-scale stress tensor, which is modeled by the dynamic eddy viscosity subgrid-scale model,

$$\tau_{ij} - \tfrac{1}{3}\tau_{kk}\delta_{ij} = -2\nu_t \overline{S}_{ij},$$

(2)

where $\overline{S}_{ij}$ is the filtered strain-rate tensor and ν_t is the eddy viscosity calculated by

$$\nu_t = C\Delta^2|\overline{S}|,$$

(3)

where C is the model coefficient calculated dynamically using the procedure of Germano *et al.* [60], $|\overline{S}| = \sqrt{2\overline{S}_{ij}\overline{S}_{ij}}$, and $\Delta = J^{-1/3}$ is the filter size, where J^{-1} is the cell volume.

The governing equations are spatially discretized using a second-order accurate central differencing scheme, and integrated in time using the fractional step method. An algebraic multigrid acceleration along with generalized minimal residual method (GMRES) solver is used to solve the pressure Poisson equation. A matrix-free Newton-Krylov method is used for solving the discretized momentum equation. More details about the flow solver can be found in Refs. [50,61,62].

The three different periodic hill geometries with varying slopes considered in this work are depicted in Fig. 1. The baseline geometry is shown in Fig. 1(a) with the computational domain and the employed curvilinear mesh on a x-y plane, which has been extensively employed in experiments [46,47] and numerical simulations [42,43,48]. Different slopes of the hill are obtained by multiplying a factor to the width of the hill as in the literature from Xiao *et al.* [49], shown in Appendix A. As seen, for the baseline geometry, the height of the hill is h, with a flat wall placed $2.036h$ above the crest of the hill, and the distance between the crests of two hills is $L_x = 9h$. In the spanwise direction, the size of the computational domain is $L_z = 4.5h$ for all the cases. The Reynolds number based on the bulk velocity U_b, which is defined as $U_b = Q/[\rho L_z(L_y - h)]$ (where Q is the mass flux), and the height of the hill is $\mathrm{Re}_h = \rho U_b h/\mu$. No slip boundary condition is applied at the top wall and the surface of the hills. In the streamwise and spanwise directions, periodic boundary condition is applied. The flow is driven by a pressure gradient uniformly applied to whole domain to maintain a constant mass flux.

In this work, the WRLES of flow over periodic hills at three Reynolds numbers are carried out for the training and testing of data-driven wall model, as shown in Table I. For $\mathrm{Re}_h = 5600$
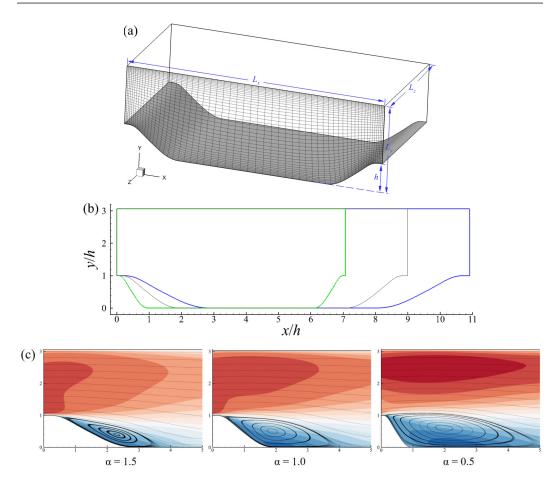
FIG. 1. Schematic of the periodic hill geometry with different steepness and the time-averaged flow fields for (a) the baseline periodic hill geometry with computational domain ($L_x = 9.0h$, $L_y = 3.036h$, $L_z = 4.5h$) and the employed curvilinear mesh on a x-y plane (on which every fifth grid line is displayed), (b) schematic of different hill geometries obtained by multiplying a factor α to the width of the baseline geometry (grey line) for the green line $\alpha = 0.5$ and the blue line $\alpha = 1.5$, respectively, and (c) the contours of time-averaged streamwise velocity and streamlines from the WRLES case at $Re_h = 10595$ for different values of α.

and 19 000, only the baseline geometry is considered, while for $Re_h = 10\,595$, simulations with all three geometries are carried out. The data sets from cases 1 and 3 are employed for training the data-driven wall model, with others for model testing. The computational domain of flow over periodic hills is discretized using a body-fitted curvilinear grid, as shown in Fig. 1(a). The height of the first off-wall grid nodes in wall units, $\Delta y^+ = \Delta y_{cc} u_\tau / \nu$, is in the range of 0.056 to 3.95 at $Re_h = 10595$ as shown in Fig. 17 in Appendix B. Here, $\Delta y_{cc} = \Delta y/2$ is half the height of the first off-wall grid, $u_\tau = \sqrt{\tau_w/\rho}$ denotes the friction velocity, and $\nu = \mu/\rho$.

The size of time step is $\Delta t = 0.01h/U_b$. The simulation is first carried out for about $22T$ (flow-through time $T = L_x/U_b$) for the flow to achieve a fully developed state. Then the flow is further simulated for about $50T$ for time-averaged quantities and flow-field data on slices for training the data-driven wall model.

To validate the employed numerical method and case setup, we compare the profiles of the mean velocity, Reynolds shear stress, turbulence kinetic energy, and the skin friction and pressure coefficients computed in this work with the results from measurements [43] and DNS by Krank

TABLE I. Parameters for the WRLES cases carried out in this work, where α denotes different hill geometries (Fig. 1) and Δy_{cc} is the height of the first off-wall grid node.

Case	Re_h	Mesh ($N_x \times N_y \times N_z$)	α	Δt	$\Delta y_{cc}/h$
1	5600	$297 \times 193 \times 187$	1.0	0.01	0.0015
2 (Hill_S)	10595	$267 \times 193 \times 187$	0.5	0.01	0.0015
3	10595	$297 \times 193 \times 187$	1.0	0.01	0.0015
4 (Hill_L)	10595	$327 \times 193 \times 187$	1.5	0.01	0.0015
5	19000	$460 \times 300 \times 290$	1.0	0.005	0.00075

et al. [48] and demonstrate an overall good agreement as shown in Appendix B for validating the employed numerical method and case setup.

B. Data preparation

The WRLES data are further processed to prepare the data for training the data-driven wall model. In WMLES, the wall shear stress is often computed using the velocity at the first off-wall grid node or nodes further away from the wall to avoid the log-layer mismatch [63]. If the data-driven model is developed using the velocity at a specific location, it may only be applicable to grids of fixed grid spacing. Moreover, if the wall model is developed using the data at a certain streamwise location, e.g., the location where the flow is attached or the location where flow separation occurs, it may only be valid for a certain flow condition. To avoid these two issues, we are devoted to develop a data-driven wall model applicable to different spatial resolutions and not limited to certain flow conditions using the data in the near-wall region of the periodic hills at all streamwise locations. Specifically in this work, the flow data in the near-wall region with wall-normal distance in the range of $0.006 \leqslant \eta/h \leqslant 0.1$ are employed, where η denotes the wall-normal coordinate. The top boundary of the region at $\eta/h = 0.1$ is determined considering that the flow field above is less correlated with the wall shear stress and is usually well-resolved by WMLES. It is noticed that the region with $\eta/h < 0.1$ is defined as the inner layer for a turbulent channel flow, where h is the half width of the channel. The bottom boundary at $\eta/h = 0.006$ is defined to preclude the effects of viscous sublayer and with the consideration that no wall model is needed if the viscous scale is resolved.

A step-by-step diagram for preparing the training data is shown in Fig. 2. Saving the three-dimensional flow fields at every time step, which requires a significant amount of disk space, is not feasible. Instead, we save the WRLES data at four spanwise (x-y) slices located at $z/h = 0.0$, 1.125, 2.25, and 3.375, respectively. To make the most of the WRLES data and meanwhile keep the cost for training the model at a reasonable level (in other words, avoid using the flow fields close in time, which can be very similar), nine snapshots of the instantaneous flow fields are extracted on each slice for one flow-through time. In total, we obtain 450 snapshots for all 50 flow-through times at each Reynolds number. It is preferred that the data in z and t employed for model training are independent from each other. To examine such independence, the correlation coefficient between two successive snapshots and the correlation coefficient between two neighbor spanwise slices are computed, which are approximately 0.5 and zero, respectively.

For each snapshot, the flow-field data at different wall-normal locations are further extracted at $N_x - 1$ streamwise locations due to periodic boundary condition to include different flow features along the lower wall of periodic hills. At each streamwise location of the lower wall, the flow-field data at 95 nodes uniformly distributed in $\eta/h \in [0.006, 0.1]$ are interpolated from the surrounding grid nodes to form 95 pairs of input-output data along the wall-normal direction. Finally, the flow-field data along the wall-normal direction at different streamwise locations for all considered spanwise slices and snapshots form the complete training and testing data sets, which contain approximately 1.8×10^8 input-output pairs. It is noticed that the grid nodes in the wall-normal
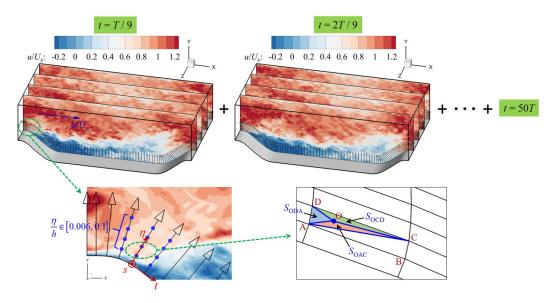
FIG. 2. Schematic diagram of the data preparation from the WRLES data for training the data-driven wall model. To prepare the data, 450 snapshots covering 50 flow-through times are extracted on four x-y slices located at $z/h = 0.0$, 1.125, 2.25, and 3.375. At each snapshot, the flow-field data at 95 locations along the wall-normal direction in the region $0.006 \leqslant \eta/h \leqslant 0.1$ are extracted at $N_x - 1$ streamwise locations using the triangulation with linear interpolation approach.

(η) direction in general do not coincide with the curvilinear grid nodes employed for solving the flow. The linear interpolation approach based on triangulation is employed to obtain the flow-field data at the 95 points along the wall-normal coordinate.

Input features and output labels are critical for the success of data-driven models. The wall shear stress including the streamwise and spanwise stresses $\tau_{w,t}$, $\tau_{w,s}$, which are often applied as boundary conditions for outer flow simulations in WMLES, are employed as the output labels. To prepare the data set for model training, the wall shear stresses are directly calculated using the WRLES data. As for the input features, the wall-normal distance η; the three velocity components $u_{w,t}$, $u_{w,n}$, and u_s in the wall-tangential, wall-normal, and spanwise directions; and the pressure gradients $\frac{\partial p}{\partial w_t}$, $\frac{\partial p}{\partial w_n}$ in the wall-tangential and wall-normal directions are employed. It has been shown by Duprat *et al.* [45] that using a near-wall scaling defined with the classic friction velocity and the streamwise pressure gradient can improve the performance of wall models for separated flows. To take into account such knowledge when constructing the neural networks for data-driven wall models, the wall-normal distance normalized using the near-wall scale and written in the logarithmic form, i.e., $\ln(\eta/y^*)$, where $y^* = \nu/u_{\tau p}$, $u_{\tau p} = \sqrt{u_v^2 + u_p^2}$, $u_v = \sqrt{|\nu u_t/\eta|}$, $u_p = |(\mu/\rho^2)(\partial P/\partial x)|^{1/3}$, is employed as the input feature for training the data-driven wall model. It is noticed that u_v is the friction velocity only if η is located within the viscous sublayer. The same normalization is employed in both model training and the *a priori* and *a posteriori* tests. For each point, to further improve the generality of the trained model, the pressure gradients are multiplied by $\frac{\eta}{h}$ before being taken as input features as suggested by Yang *et al.* [64].

III. CONSTRUCTION OF DATA-DRIVEN WALL MODELS

A. Feedforward neural network

We use a multi-hidden-layer feedforward neural network (FNN) to establish the relation between the near-wall flow and the wall shear stress on the surface of periodic hills. As shown in Fig. 3, the
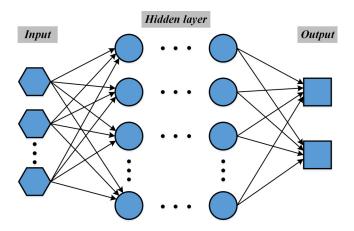
FIG. 3. Schematic diagram of the feedforward neural network (FNN) with multiple hidden layers.

employed FNN consists of an input layer, multiple hidden layers, and an output layer. Each layer has a number of neurons, which are computational units that propagate the weighted sums of the inputs to an activation function and calculate the output. The detailed procedures for calculating the output based on the input in the FNN is shown in Appendix C, which includes the linear matrix manipulation of the weight and bias coefficients and the nonlinear mapping using the activation function.

The activation function used in this paper is the rectified linear unit (ReLU) [65],

$$f(x) = \begin{cases} 0, & \text{if } x < 0, \\ x, & \text{if } x \geqslant 0. \end{cases} \tag{4}$$

The prepared input and output data are normalized using the min-max scaling,

$$x^* = \frac{x - x_{\min}}{x_{\max} - x_{\min}}. \tag{5}$$

The loss function is defined as

$$E_{\text{WM}} = \frac{1}{N_s} \sum_{i=1}^{N_s} (\mathbf{Y}_i - \mathbf{Y}_i^*)^2 + \frac{\lambda_0}{2N_s} \|w\|_2^2, \tag{6}$$

where N_s is the number of training samples, w is the weight coefficient, and λ_0 is the regularization rate, which is set to 0.001. The first term in Eq. (6) denotes the mean square error (MSE) between the FNN output $\mathbf{Y}^*$ and the labeled output $\mathbf{Y}$ from the WRLES. The second term is an L2 regularization term included to avoid overfitting.

We use the error backpropagation (BP) scheme [56] implemented with TENSORFLOW [57] to train the FNN by optimizing the weight and bias coefficients to minimize the loss function. The key steps for FNN training are as follows:

(1) Provide training data to the input layer, propagate data signal forward layer by layer, and compute the result in the output layer. Details on this step can be found in Appendix C.

(2) Compute the loss function according to Eq. (6) using FNN output and the labeled output.

(3) Adjust the weight and bias coefficients using the gradient descent algorithm,

$$v = v + \Delta v, \quad \Delta v = -\eta \frac{\partial E_{\text{WM}}}{\partial v}, \tag{7}$$

where v denotes the weight and bias coefficients in the FNN, and $\eta \in (0, 1)$ denotes the learning rate, which is dynamically adjusted using the Adam optimizer [66].

TABLE II. Two sets of cases for examining the effects of different numbers of input features (case set 1) and different number of neurons (case set 2) on training performance. In this table, "N" denotes the number of neurons and "H" denotes the number of hidden layers. For both sets of cases, we only consider one output, i.e., the wall-tangential shear stress.

	No. of inputs (no. per point × no. of points)	No. of neurons (no. of hidden layer)
Case set 1	5× (1, 2, 3, 4, 5, 6)	N20 (H6)
Case set 2	5 × 3	N3, N5, N10, N20, N50, N100 (H6)

(4) Repeat the above steps until the maximum number of training epochs is achieved or the value of the loss function is sufficiently small and does not change when increasing the number of epochs.

B. Training of the data-driven wall model

In this section, three sets of cases, i.e., one with different number of input features, another one with different number of neurons in each hidden layer, and the third one with different number of output labels, are carried out to evaluate the performance of different setups for training wall model using FNN and the flow data at $Re_h = 5600$ and $10\,595$. The key requirement for a wall model is to accurately predict the wall shear stress. In conventional wall models, the wall shear stress is determined by an empirical relation (e.g., the power law or the logarithmic law) or simplified Navier-Stokes equations (e.g., the thin boundary layer equation) using the velocity at one off-wall grid node (usually the first or the second off-wall node). To compensate for the lack of governing equations in data-driven wall models, flow-field data at more than one off-wall grid nodes probably can improve the training efficiency and predictive capability of the model. In the first set of cases, we test the effects of input features obtained using different numbers of wall-normal points (five inputs per point) with the distance between two adjacent points $0.03h$. How well a data-driven model represents near-wall turbulence with flow separations and reattachments depends on the complexity of the employed neural network, i.e., the number of hidden layers and the number of neurons in each layer. In the second set of cases, we examine the effects of the number of neurons ranging from 3 to 100 on the training performance with fixed number of hidden layers and input features. Details on these two sets of cases can be found in Table II.

Figure 4 plots the variations of loss with the training epochs for both training and validation data sets for the two sets of cases. The number of training samples is 1.24×10^7, of which 90% are used
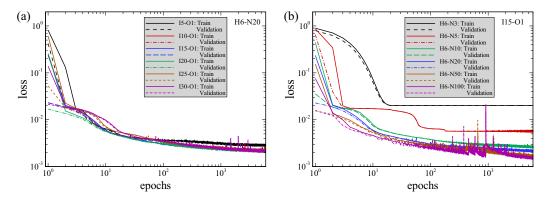

FIG. 4. The variations of loss with training epochs for both the training and validation datasets for (a) results from case set 1 with different numbers of input features and (b) results from case set 2 with different numbers of neurons. In this figure, the numbers after letters "I," "O," "H," and "N" denote the numbers of input features, output labels, hidden layers, and neurons, respectively.

TABLE III. The training of two FNN models with different inputs and outputs.

FNN	Input	Output	HL size
FNN-1	$[\ln(\eta/y^*), \frac{u_{w,t}}{h_{wm}}, \frac{u_{w,n}}{h_{wm}}, \frac{\partial p}{\partial w_t}\frac{h_{wm}}{h}, \frac{\partial p}{\partial w_n}\frac{h_{wm}}{h}] \times 3$	$\tau_{w,t}$	
FNN-2	$[\ln(\eta/y^*), \frac{u_{w,t}}{h_{wm}}, \frac{u_{w,n}}{h_{wm}}, \frac{u_s}{h_{wm}}, \frac{\partial p}{\partial w_t}\frac{h_{wm}}{h}, \frac{\partial p}{\partial w_n}\frac{h_{wm}}{h}] \times 3$	$\tau_{w,t}, \tau_{w,s}$	H6-N20

as the training data set and the remaining 10% are used as the validation data set, and the batch size is 2×10^5. Initially, the loss is large because the weight coefficients are randomly set and the bias coefficients are set to zero. Then, the weight and bias coefficients are adjusted and the loss rapidly decreases during the first few epochs. After the initial stage, the loss tends to approach a steady small value after approximately 1000 training epochs.

In Fig. 4(a), the loss in the FNN model I5-O1 (only using input features at one wall-normal point) is significantly worse than in the other models: The loss at 6000 epochs is about 1.5 times larger than others, while the values of loss from the models using input features at more than one point are similar to each other. This indicates that only using the input features at one point is not sufficient to accurately model the complex near-wall turbulence encountered in this periodic hill case, while adding just one point can significantly improve the training performance. To ensure the training performance without increasing the computational cost in the meantime, we choose 15 input features from three wall-normal points for case set 2 and other cases in this work. Figure 4(b) compares the loss of FNN models with different number of neurons. If no overfitting occurs, more neurons employed is correlated with smaller loss. In this work, we use 20 neurons for the proposed FNN wall model.

To consider the influence of output labels on the FNN training, the models FNN-1 with only one output label ($\tau_{w,t}$) and FNN-2 with two output labels ($\tau_{w,t}, \tau_{w,s}$) are trained, validated, and tested. The settings of the two FNN wall models are shown in Table III. As for the first of the input features, we did a test comparing the loss function when using $\ln(\eta/y^*)$ with that using η/y^*. It is observed that the value of loss function from the case using $\ln(\eta/y^*)$ is smaller than that from the case using η/y^*. As for the model performance, no significant improvement is observed when using $\ln(\eta/y^*)$ compared with η/y^*. Figure 5 shows the variations of loss with training epochs for FNN-1 and FNN-2. It can be observed that including the spanwise wall shear stress as the output label has some effects on the model training process for epochs less than 100 but little influence on the final loss of tangential wall shear stress.
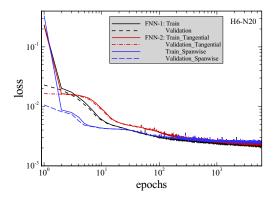

FIG. 5. The variations of loss with training epochs for both the training and validation data sets for FNN-1 and FNN-2.

IV. EVALUATION OF DATA-DRIVEN WALL MODELS

A. Accuracy test

To evaluate the prediction accuracy of the trained FNN wall model, we apply it to predict the wall shear stress for different snapshots and spanwise slices for both training data sets and testing data sets obtained from the cases with $\mathrm{Re}_h = 5600$ and 10 595.

We first evaluate the FNN wall models for predicting wall shear stresses using the training dataset. In Fig. 6, we show the comparison of the instantaneous friction coefficient (which is defined as $C_f = \tau_w / \frac{1}{2}\rho U_b^2$) at an instant, the correlation coefficient $\rho_{\text{FNN-LES}}$ between the instantaneous wall shear stress predicted by the FNN model and the WRLES, and the error ε_τ of the instantaneous wall shear stress predicted by the FNN model relative to the WRLES predictions. Here, the correlation coefficient ρ_τ is defined as

$$\rho_\tau = \frac{\left\langle \left(\tau_w^{\text{FNN}} - \left\langle \tau_w^{\text{FNN}} \right\rangle \right)\left(\tau_w^{\text{LES}} - \left\langle \tau_w^{\text{LES}} \right\rangle \right) \right\rangle}{\left\langle \left(\tau_w^{\text{FNN}} - \left\langle \tau_w^{\text{FNN}} \right\rangle \right)^2 \right\rangle^{1/2} \left\langle \left(\tau_w^{\text{LES}} - \left\langle \tau_w^{\text{LES}} \right\rangle \right)^2 \right\rangle^{1/2}}, \tag{8}$$

where $\langle \rangle$ denotes the average over snapshots.

To further assess the prediction accuracy of FNN model on the fluctuations of wall shear stress over time, we define the instantaneous relative error ε_τ as follows:

$$\varepsilon_\tau = \left\langle \frac{\left| \tau_w^{\text{FNN}} - \tau_w^{\text{LES}} \right|}{\left| \left\langle \tau_w^{\text{LES}} \right\rangle \right|_{\max}} \right\rangle, \tag{9}$$

where $\left| \left\langle \tau_w^{\text{LES}} \right\rangle \right|_{\max}$ denotes the peak value of averaged wall shear stress among all the streamwise locations. The relative error of the time-averaged wall shear stress, which will be shown in Fig. 7(d), is defined as follows:

$$\varepsilon_{\langle \tau \rangle} = \frac{\left\langle \tau_w^{\text{FNN}} \right\rangle - \left\langle \tau_w^{\text{LES}} \right\rangle}{\left| \left\langle \tau_w^{\text{LES}} \right\rangle \right|_{\max}}. \tag{10}$$

As seen in Figs. 6(a) and 6(b), the instantaneous skin friction coefficient C_f predicted by the FNN model in general agrees with that from WRLES at most streamwise locations. Many sharp peaks are observed in streamwise variation of the instantaneous wall shear stress. The trained FNN wall model is observed being able to predict these abrupt variations at most streamwise locations, although the peak amplitude is underpredicted at some locations, e.g., at $x/h \approx 0.18$ for this instant for the $\mathrm{Re}_h = 10\,595$ case. It is also noticed that the wall-tangential component of wall shear stress predicted by the FNN-1 and FNN-2 almost collapse with each other. Moreover, the spanwise component of the wall stress predicted by the FNN-2 model is also in good agreement with the WRLES predictions. In Figs. 6(c)–6(d), it is observed that the correlation coefficients are larger than 0.7 and the instantaneous relative errors are smaller than 0.1 at almost all streamwise locations except near the crest of the hill at $x/h = 0.2$ and $x/h = 8.5$ (where the correlation coefficient is around 0.6 and the instantaneous relative error is around 0.15), indicating that the large temporal fluctuations there are not well captured by the FNN model. It is noticed that correlation coefficient for the spanwise wall shear stress is similar with that of the tangential wall shear stress although the magnitude of the instantaneous spanwise wall shear stress is one order of magnitude smaller than the tangential component, which makes it difficult to train the corresponding FNN model for both components.

In Fig. 7, we evaluate the capability the FNN model in predicting the mean wall shear stress and the standard deviation of wall shear stress. As seen in Fig. 7(a), the mean skin friction coefficients at both $\mathrm{Re}_h = 5600$ and 10 595 predicted by the FNN models (i.e., FNN-1 and FNN-2) are in perfect agreement with WRLES results at all streamwise locations. The mean spanwise wall shear stress component, on the other hand, is close to zero for both FNN-2 and WRLES predictions (not shown in the figure). In Figs. 7(b) and 7(c), we compare the normalized standard deviations of the
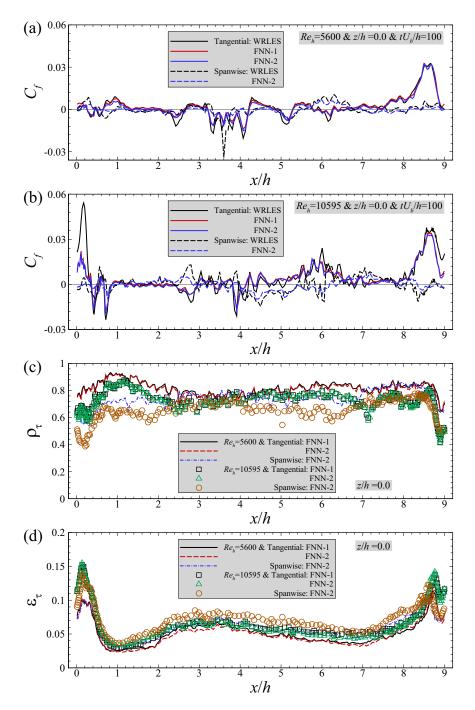
FIG. 6. Evaluation of the FNN wall model using the training data set for [(a), (b)] comparison of instantaneous skin friction coefficients computed by different FNN wall models with that from WRLES; (c) correlation coefficients [Eq. (8)] of instantaneous wall shear stresses between the predictions from the FNN wall models and the WRLES; (d) relative error [Eq. (9)] for different FNN wall models for instantaneous snapshots on the x-y slice located at $z/h = 0.0$.
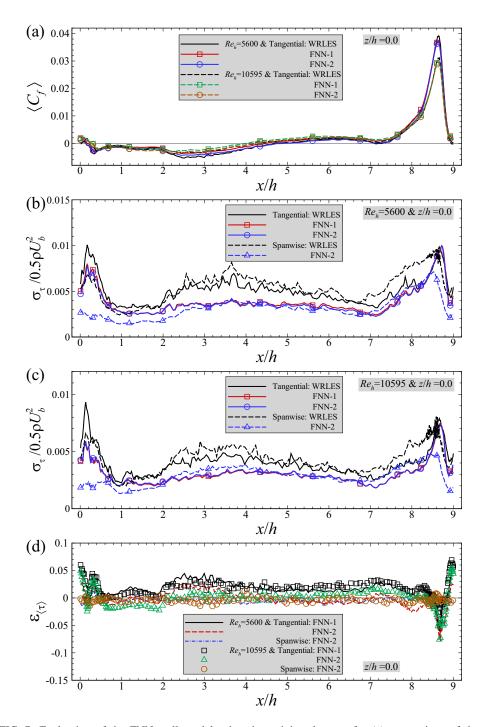
FIG. 7. Evaluation of the FNN wall model using the training data set for (a) comparison of the time-averaged skin friction coefficients computed by different FNN wall models with that from WRLES; [(b), (c)] normalized standard deviations of the wall shear stresses computed by the FNN models and the WRLES; and (d) relative error [Eq. (10)] based on the time-averaged wall shear stress for different FNN wall models on the x-y slice located at $z/h = 0.0$.

temporal fluctuations of wall shear stresses predicted by the FNN models with those from WRLES. It is observed that the FNN predictions are smaller than the WRLES predictions for both tangential and spanwise components. Interestingly, it is observed that the standard deviation of the spanwise shear stress is similar with the tangential component although its instantaneous value is one order of magnitude smaller than the tangential component. Figure 7(d) shows the error of time-averaged wall shear stress predicted by the FNN model relative to that from WRLES. It is seen that the absolute values of the errors are smaller than 0.05 at most streamwise locations, except at locations close to the crest of the hill.

Overall, we have shown that both FNN-1 and FNN-2 wall models can accurately predict the instantaneous and time-averaged wall shear stresses for the training data set. Next, we will evaluate the performance of the FNN wall models using the testing data set, which is obtained from a different x-y slice (located at $z/h = 2.25$) from the cases with $\mathrm{Re}_h = 5600$ and 10 595 from the training data set.

In Fig. 8, we first evaluate the capability of the FNN models in predicting the instantaneous wall shear stress using the testing data set. As seen in Figs. 8(a) and 8(b), both tangential and spanwise instantaneous skin friction coefficients predicted by the FNN models are in an overall good agreement with the WRLES predictions except for some sharp peaks. Figures 8(c) and 8(d) show the correlation coefficient and relative error between the FNN and LES predictions. As seen in the range of $x/h = 1$ to 8.5, the correlation coeffcients are in general larger than 0.7 and the relative errors are smaller than 0.1 for both tangential and spanwise components. At locations close to the crest of the hill, lower coefficients and larger errors are observed especially close the separation point for the spanwise component.

In Fig. 9, we compare the mean skin friction coefficients (averaged over snapshots), the standard deviations of the fluctuations and the time-averaged relative error of wall shear stresses predicted by different FNN wall models. As seen in Fig. 9(a), good agreements between the FNN and WRLES predictions at $\mathrm{Re}_h = 5600$ and 10 595 are obtained for the mean friction coefficients for both FNN models. For the standard deviations of the wall shear stresses, the predictions by the FNN models are significantly smaller than those from WRLES for both tangential and spanwise components. In Fig. 9(d), the relative errors are smaller than 0.05 at most streamwise locations, which are close to the results in the training data set.

B. *A priori* test of FNN wall model

To further evaluate the generalization capacity of the FNN wall model, we perform the *a priori* test of the FNN wall models using cases with different Reynolds numbers and hill geometries.

First, the trained FNN wall models are applied to the testing data set at $\mathrm{Re}_h = 19\,000$.

Figures 10 and 11 evaluate the predictive capability of the FNN models on the instantaneous and mean wall shear stresses, respectively. We first examine the predictions of the instantaneous skin friction coefficient. As shown in Fig. 10(a), the FNN predictions are consistent with those from WRLES at most streamwise locations. The correlation coefficients [Fig. 10(b)] of instantaneous wall shear stresses between the FNN and LES predictions are also observed to be in general larger than 0.6, in the range of $x/h = 1$ to 8.5, although they are somewhat smaller than those computed using the training data set. The instantaneous relative errors are then examined in Fig. 10(d). It is observed that the magnitude of the errors are slightly larger than those in training data set, but still smaller than 0.1 at most streamwise locations.

Here we examine the performance of the FNN models for predicting the mean skin friction coefficient. As seen in Fig. 11(a), the mean skin friction coefficients at $\mathrm{Re}_h = 19\,000$ predicted by the FNN-2 model are in good agreement with WRLES results at all streamwise locations. Some discrepancies are observed between the FNN-1 predictions and the WRLES predictions, highlighting the importance of having spanwise wall shear stress as one of the output labels. As expected, the mean spanwise wall shear stress component is close to zero for both FNN model predictions and WRLES predictions. Similar with those observed in the cases with $\mathrm{Re}_h = 5600$ and
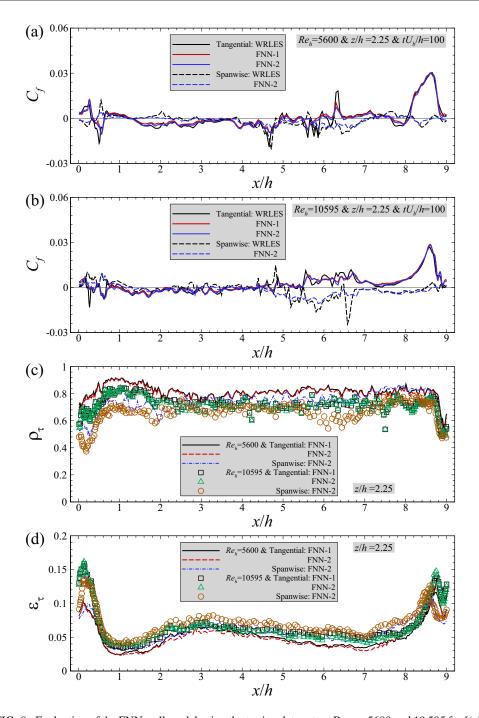
FIG. 8. Evaluation of the FNN wall model using the testing data sets at $\mathrm{Re}_h = 5600$ and $10\,595$ for [(a), (b)] comparison of instantaneous skin friction coefficients computed by different FNN wall models with that from WRLES; (c) correlation coefficients of instantaneous wall shear stresses between the predictions from the FNN wall models and the WRLES predictions; (d) relative error for different FNN wall models for instantaneous snapshots on the x-y slice located at $z/h = 2.25$.
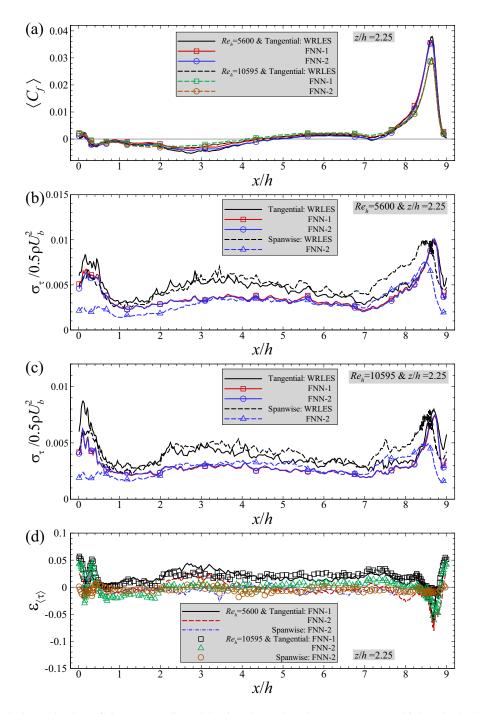
FIG. 9. Evaluation of the FNN wall model using the testing data sets at $\mathrm{Re}_h = 5600$ and 10 595 for (a) comparison of the time-averaged skin friction coefficients computed by different FNN wall models with that from WRLES; [(b), (c)] normalized standard deviations of the wall shear stresses computed by the FNN models and the WRLES; and (d) relative error based on the time-averaged wall shear stress for different FNN wall models on the x-y slice located at $z/h = 2.25$.
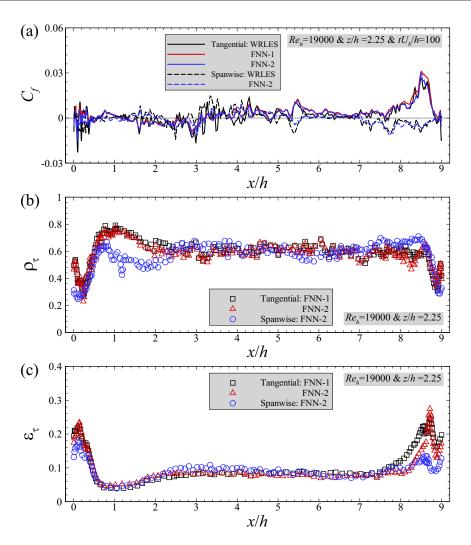
FIG. 10. Evaluation of the FNN wall model using the testing dataset at $\mathrm{Re}_h = 19\,000$ for (a) comparison of instantaneous skin friction coefficients computed by different FNN wall models with that from WRLES; (b) correlation coefficients of instantaneous wall shear stresses between the predictions from the FNN wall models and the WRLES predictions; and (c) relative error for different FNN wall models for instantaneous snapshots on the x-y slice located at $z/h = 2.25$.

10 595, the normalized standard deviations of wall shear stress fluctuations predicted by the FNN models are smaller than those from WRLES, as shown in Fig. 11(b). In Fig. 11(d), the relative errors of the time-averaged wall shear stress are smaller than 0.1 at most streamwise locations, which are slightly larger than those computed using the training data set. It is also noticed that the magnitude of the relative error for the predictions from the FNN-2 model is smaller than that from the FNN-1 model especially at locations around $x/h = 8.4$.

At last, we present the evaluation results for cases with different hill geometries. The length of the separation bubble increases as the hill becomes steeper (shown in Fig. 1). For these cases, the performance of the FNN-2 model is observed to be better than that of the FNN-1 model, with the results from the latter not presented in this paper. In Fig. 12, it is seen that the FNN-2 model accurately predicts the mean skin friction coefficients although the peak value of C_f is somewhat
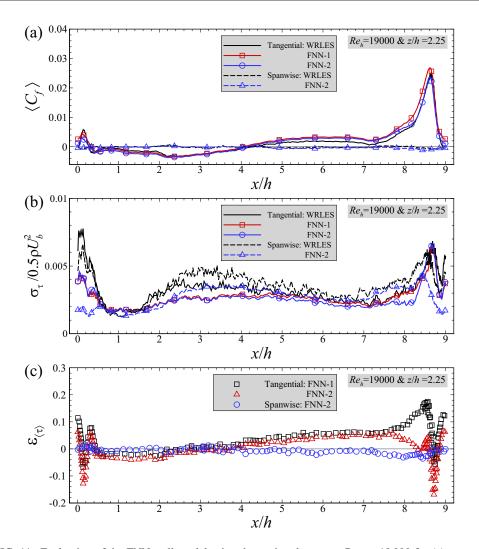
FIG. 11. Evaluation of the FNN wall model using the testing data set at $Re_h = 19\,000$ for (a) comparison of the time-averaged skin friction coefficients computed by different FNN wall models with that from WRLES; (b) normalized standard deviations of the wall shear stresses computed by the FNN models and the WRLES; and (c) relative error based on the time-averaged wall shear stress for different FNN wall models on the x-y slice located at $z/h = 2.25$.

underpredicted for the hill geometry with $\alpha = 0.5$, with the relative errors between the predictions from the FNN-2 model and the WRLES of less than 0.1 except for the location close to the hilltop on the windward side, as shown in Fig. 12(c). In Fig. 12(b), it is seen that the correlation coefficients of the instantaneous wall shear stress between the predictions from the FNN model and the WRLES are in general larger than 0.6. These evaluation results demonstrate the good generalization capacity of the trained FNN wall models for different hill geometries with different separation patterns.

C. *A posteriori* test of FNN wall model

In this section, the trained FNN wall model is evaluated in the actual WMLES, i.e., *a posteriori* test, where the velocity and pressure computed in WMLES are employed as the input features
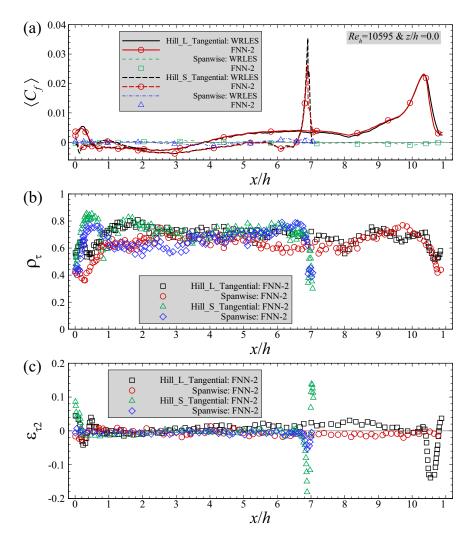
FIG. 12. Evaluation of the FNN wall model for cases with different hill geometries for (a) comparison of the time-averaged skin friction coefficients computed by the FNN models with that from WRLES, (b) correlation coefficients of the instantaneous wall shear stresses between the predictions from the FNN wall models and the WRLES, and (c) relative error of the time-averaged wall shear stress for the FNN wall models on the x-y slice located at $z/h = 0.0$.

in the FNN wall model with the predicted wall shear stress in turn affecting the solution of the WMLES. In the present WMLES, the wall shear stress and the nonpenetration boundary conditions are employed for the wall-parallel and wall-normal velocity components, respectively. Two different wall models are considered, i.e., the FNN wall model developed in this work and the Werner-Wengle (WW) model [67]. Details of the implemented WW model can be found in Appendix D. In the WW model, the velocity at the first off-wall grid node is employed for computing the wall shear stress. In the FNN wall model, the input features computed at y_f, $y_f + 0.03h$, and $y_f + 0.06h$ away from the wall are employed for computing the wall shear stress.

Two cases are considered, the flow over periodic hills, which is the major objective of this work, and the turbulent channel flow, which is simple with no flow separation and reattachment but challenging because the turbulent channel flow data are not employed for training the FNN model.
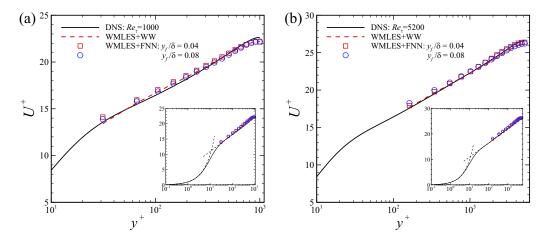
FIG. 13. Comparison of the mean streamwise velocity obtained from WMLES with different wall models with DNS for turbulent channel flows for (a) $Re_\tau = 1000$ and (b) $Re_\tau = 5200$ (the DNS data are from the Johns Hopkins turbulence databases [68]).

1. Turbulent channel flow

In this subsection, we evaluate the predictive capability of the developed FNN wall model in simulating the turbulent channel flows.

The dimensions of the channel are 7.0δ, 2.0δ, and 3.5δ in the streamwise, vertical, and spanwise directions, respectively, where δ is the half-height of the channel. Two different Reynolds numbers are considered, i.e., $Re = U_b\delta/\nu = 19\,999$ and 1.25×10^5, where U_b is the bulk velocity, which correspond to the Reynolds number based on the friction velocity, $Re_\tau = u_\tau\delta/\nu = 1000$ and 5200, respectively. In WMLES, the channel is discretized with a computational mesh of $32 \times 32 \times 32$, and the height of the first off-wall grid is set to $\delta/32$.

Figures 13–15 compare the vertical profiles of mean streamwise velocity, the primary Reynolds shear stress, and turbulent intensities obtained from WMLES with different wall models and the
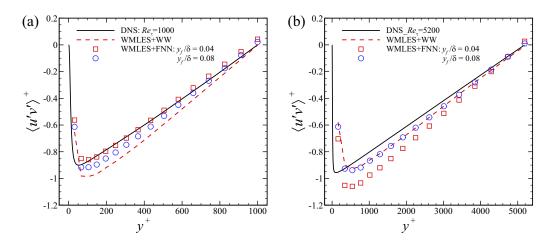

FIG. 14. Comparison of the vertical profiles of the primary Reynolds shear stress $\langle u'v' \rangle^+$ obtained from the WMLES with different wall models with DNS for turbulent channel flows for (a) $Re_\tau = 1000$ and (b) $Re_\tau = 5200$.
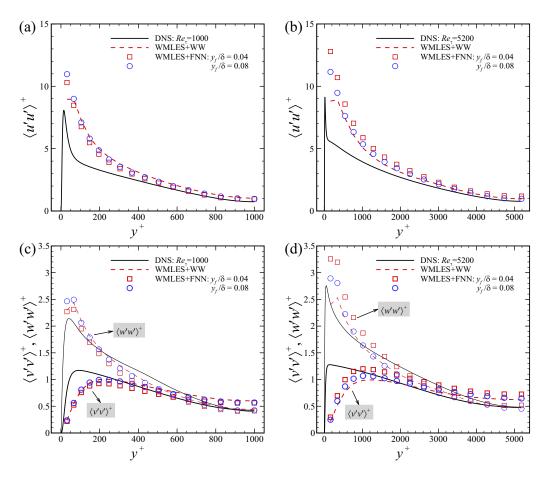
FIG. 15. Comparison of the vertical profiles of $\langle u'u'\rangle^+$, $\langle v'v'\rangle^+$, and $\langle w'w'\rangle^+$ obtained from the WMLES with different wall models with DNS for turbulent channel flows for [(a), (c)] $\mathrm{Re}_\tau = 1000$ and [(b), (d)] $\mathrm{Re}_\tau = 5200$.

DNS data for $\mathrm{Re}_\tau = 1000$ and 5200. For the FNN wall model, two different cases are considered with the first interpolation point located at different locations from the wall, i.e., $y_f/\delta = 0.04, 0.08$. The profiles of DNS are downloaded from the Johns Hopkins turbulence databases [68], reported by Lee and Moser [69]. As shown in Fig. 13, the mean streamwise velocities predicted by the FNN and the WW wall models agree well with those from the DNS. As for the primary Reynolds shear stress shown in Fig. 14, the FNN wall model gives better predictions than the WW model for the case with $\mathrm{Re}_\tau = 1000$, but overestimates the magnitude for the case with $\mathrm{Re}_\tau = 5200$. For the turbulence intensities shown in Fig. 15, the results from the FNN wall model are in good agreement with those from the WW model, while both of them overestimate the streamwise and spanwise components and underestimate the vertical component in the near-wall region, respectively, when compared to the DNS results. In the outer region, the predictions from the WMLES with the FNN wall model are in better agreement with the DNS results. Furthermore, it is observed that the predictions from the FNN wall model with different y_f are minor for different components of turbulence intensities.

2. The flow over periodic hills

In this subsection, we present the *a posteriori* test of the FNN wall model for the flow over periodic hills. Only the case at $\mathrm{Re}_h = 10\,595$ with the baseline geometry is considered. The number
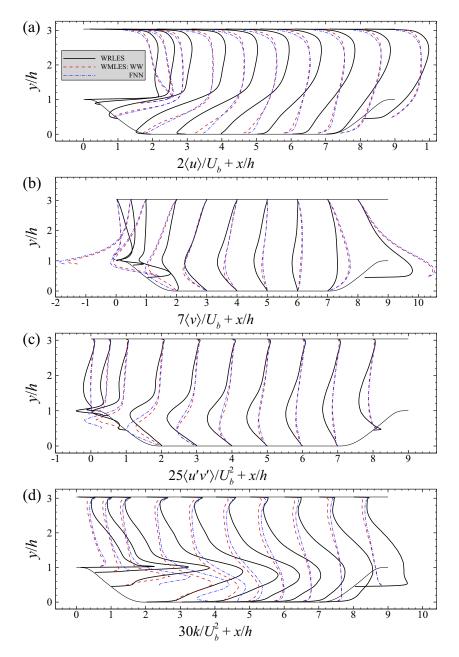
FIG. 16. Comparison of vertical profiles from the WMLES with WW and FNN wall models and the WRLES of flow over periodic hills for (a) time-averaged streamwise velocity $\langle u \rangle$, (b) time-averaged vertical velocity $\langle v \rangle$, (c) primary Reynolds shear stress $\langle u'v' \rangle$, and (d) turbulence kinetic energy $k = \frac{1}{2}\langle u'u' + v'v' + w'w' \rangle$.

of grid nodes is $N_x \times N_y \times N_z = 112 \times 32 \times 64$. The grid spacings near the crest of the hill are $\Delta x/h = 0.08$ and $\Delta y/h = 0.03$ in the streamwise and vertical directions, respectively.

Figure 16 compares the vertical profiles of turbulent statistics from the WMLES with WW and FNN wall models with the WRLES results. The FNN wall model is applied to both the lower and

upper walls. Large discrepancies are observed for the profiles of velocity, Reynolds shear stress, and turbulence kinetic energy at different streamwise locations for both wall models for the employed grid.

There are several different reasons causing the poor performance of the FNN wall model in the *a posteriori* test of the periodic hill case. First, the input features, i.e., the instantaneous velocity and pressure field in the near-wall region, from the WMLES are different from those from the WRLES. The instantaneous flow fields from WMLES, which are affected by the SGS model, the wall model, the grid resolution, the discretization schemes, and others, are not the same as the filtered instantaneous flow fields from WRLES. Second, only using the wall shear stress boundary condition for the outer flow may not be enough for the periodic hill case. Near the region of flow separation or reattachment, the wall shear stress, which is close to zero, probably cannot fully represent the effect of near-wall layer on the outer flow. Because of the coupling of the FNN wall model with the outer flow, it is not easy to examine the two reasons separately.

V. CONCLUSION

As a first step toward developing a general wall model for complex turbulent flows, in this work we developed a data-driven wall model for LES of flow over periodic hills using the physics-informed feedforward neural networks and WRLES data.

Data preparation is critical for the success of training data-driven wall models. As the objective of this work is to develop a wall model that is applicable to different streamwise locations (of different flow regimes, i.e., attached wall turbulence, flow separation, and reattachment) of the periodic hill, the flow data near the surface of the hill at all streamwise locations are grouped together as the training data. The wall shear stresses are taken as the output labels. The input features include wall-normal distance and different components of velocity and pressure gradient at different wall-normal locations.

Effects of number of input features and number of neurons in the hidden layers on training performance were tested. It was found that using the flow data at more than two off-wall locations (in addition to the velocity at the boundary, which is implicitly taken into account) are adequate for training the data-driven wall model. Further increasing the number of input features does not improve the convergence rate when training the model. Employing more than 20 neurons in each hidden layer is found enough for this case. In the data-driven model developed in this work, flow data at three off-wall locations are employed as input features with 20 neurons for each hidden layer. Two different wall models, i.e., one using only the tangential wall shear stress as the output label (FNN-1), and the other one using both wall shear stress components as the output labels (FNN-2), are tested.

The prediction accuracy and generalization capacity of the trained FNN wall model were examined by comparing the predicted wall shear stresses with the WRLES data. The instantaneous wall shear stresses predicted by the FNN wall model show an overall good agreement with the WRLES data with some discrepancies observed at locations near the crest of the hill. For the mean wall shear stress, the predictions from the FNN wall models agree very well with WRLES data. However, the standard deviations of the fluctuations of the wall shear stress are underpredicted by the FNN wall model. Furthermore, it is noticed that the predictions from the two models, i.e., FNN-1 and FNN-2, are very similar with each other for the $\mathrm{Re}_h = 5600$ and 10 595 cases, which are employed for training the model. For the $\mathrm{Re}_h = 19\,000$ case and the cases with different hill geometries, for which the flow data are not employed for training the model, the FNN-2 model is observed performing better than the FNN-1 model. In summary, good performance and generalization capacity are observed in the *a priori* test of the developed FNN wall models.

Finally, the FNN wall model is applied to the WMLES of flow over periodic hills and turbulent channel flows, as the *a posteriori* test. For the turbulent channel flow cases, overall good agreements are obtained for the mean streamwise velocity, the primary Reynolds shear stress, and the turbulent intensities. For the flow over periodic hills, discrepancies between the FNN predictions and the

WRLES data are observed for different flow quantities. Reasons causing this poor performance are analyzed. An in-depth analysis on this issue, which is being carried out, will be presented in our future paper.

APPENDIX A: DETAILS OF THE HILL GEOMETRY

The coordinates of the baseline hill geometry consists of six segments, described by the following piecewise functions [49,70]:

$$
\hat{y} = \begin{cases}
\min(1, 1 + 2.42 \times 10^{-4}\hat{x}^2 - 7.588 \times 10^{-5}\hat{x}^3), & \hat{x} \in [0, 0.3214], \\
0.8955 + 3.484 \times 10^{-2}\hat{x} - 3.629 \times 10^{-3}\hat{x}^2 + 6.749 \times 10^{-5}\hat{x}^3, & \hat{x} \in [0.3214, 0.5], \\
0.9213 + 2.931 \times 10^{-2}\hat{x} - 3.234 \times 10^{-3}\hat{x}^2 + 5.809 \times 10^{-5}\hat{x}^3, & \hat{x} \in [0.5, 0.7143], \\
1.445 - 4.927 \times 10^{-2}\hat{x} + 6.95 \times 10^{-4}\hat{x}^2 - 7.394 \times 10^{-6}\hat{x}^3, & \hat{x} \in [0.7143, 1.071], \\
0.6401 + 3.123 \times 10^{-2}\hat{x} - 1.988 \times 10^{-3}\hat{x}^2 + 2.242 \times 10^{-5}\hat{x}^3, & \hat{x} \in [1.071, 1.429], \\
\max(0, 2.0139 - 7.18 \times 10^{-2}\hat{x} + 5.875 \times 10^{-4}\hat{x}^2 + 9.553 \times 10^{-7}\hat{x}^3), & \hat{x} \in [1.429, 1.929],
\end{cases}
$$
(A1)

where $\hat{x} = x/h$ and $\hat{y} = y/h$ are normalized horizontal and vertical coordinates, respectively.

As for the hill geometries with varying slopes, the variables $\hat{x}$ are substituted with $\hat{x}/\alpha$ in Eq. (A1). The hill geometries in Fig. 1 are obtained from setting $\alpha = 0.5, 1.0$, and 1.5 and the fixed interhill distance ($5.142h$) of the bottom flat wall.

APPENDIX B: DETAILS ON THE EMPLOYED GRID AND VALIDATION OF THE PRESENT WRLES CASE

In this Appendix, we show some details on the employed grid and validate the employed VFS-WIND code and the case setup for simulating turbulent flows over periodic hills at $\mathrm{Re}_h = 10595$ by comparing our WRLES results with the DNS results by Krank *et al.* [48] ($896 \times 448 \times 448$ grid points). Figure 17 shows the distribution of the grid spacings in wall units for x and y direction along the lower wall, where $\Delta x^+ = \Delta x u_\tau / \nu$ denotes the streamwise grid spacing in wall unit. The height of the first off-wall grid nodes in wall units, Δy^+, is in the range of 0.056 to 3.95.
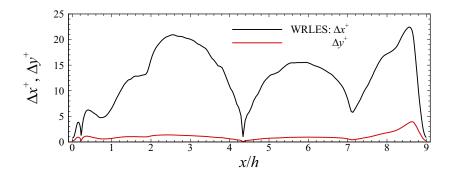

FIG. 17. Distribution of the grid spacings in wall units for x and y direction along the lower wall.
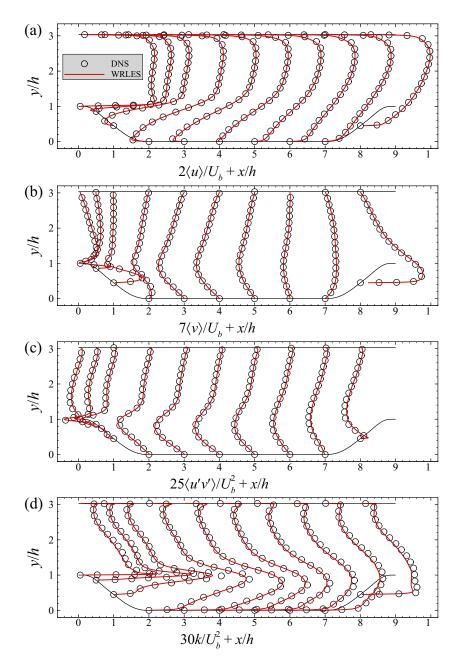
FIG. 18. Comparison of vertical profiles from the present WRLES with DNS data from Krank *et al.* [48] for (a) time-averaged streamwise velocity $\langle u \rangle$, (b) time-averaged vertical velocity $\langle v \rangle$, (c) primary Reynolds shear stress $\langle u'v' \rangle$, and (d) turbulence kinetic energy $k = \frac{1}{2}\langle u'u' + v'v' + w'w' \rangle$.

In Fig. 18, we plot the vertical profiles of the time-averaged streamwise velocity $\langle u \rangle$ and vertical velocity $\langle v \rangle$, primary Reynolds shear stress $\langle u'v' \rangle$, and turbulence kinetic energy k. As seen, the WRLES results are in good agreement with the DNS results [48] except for some minor differences observed in the Reynolds shear stress and the turbulence kinetic energy (with the relative error less than 12%). Figure 19 shows the comparison of the skin friction coefficient C_f and the pressure
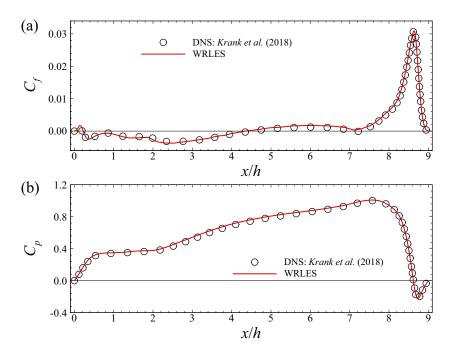
FIG. 19. Comparison of (a) skin friction coefficient and (b) pressure coefficient at the lower wall between the present WRLES and DNS by Krank *et al.* [48].

coefficient C_p. Again, the C_f and C_p from the present WRLES agree very well with the DNS predictions.

APPENDIX C: FEEDFORWARD NEURAL NETWORK

The detailed procedures for calculating the output based on the input in the FNN are described in this Appendix.

The input layer is

$$\mathbf{X} = \left[x_1, x_2, \ldots, x_{n_I}\right]^{\mathrm{T}}, \tag{C1}$$

where x_i denotes the ith input feature and n_I is the number of neurons in the input layer. The matrices of weight and bias coefficient connecting the input layer and the hidden layer are

$$\mathbf{W}^1 = \begin{bmatrix} w_{1,1}^1 & w_{1,2}^1 & \cdots & w_{1,n_I}^1 \\ w_{2,1}^1 & w_{2,2}^1 & \cdots & w_{2,n_I}^1 \\ \vdots & \vdots & \ddots & \vdots \\ w_{n_H,1}^1 & w_{n_H,2}^1 & \cdots & w_{n_H,n_I}^1 \end{bmatrix}, \quad \mathbf{B}^1 = \begin{bmatrix} b_1^1 \\ b_2^1 \\ \vdots \\ b_{n_H}^1 \end{bmatrix}, \tag{C2}$$

where $w_{i,j}^1 (i = 1, 2, \ldots, n_H; j = 1, 2, \ldots, n_I)$ denotes the weight coefficient connecting the ith neuron in the hidden layer and the jth neuron in the input layer, b_i^1 denotes the bias coefficient for the ith neuron in the hidden layer, n_H is the number of neurons in the hidden layer. Initially, the weight coefficients are set to be random numbers from truncated normal distribution (0.0 mean and 0.1 standard deviation) and the bias coefficients are set to zero.

The output of the hidden layer is

$$\mathbf{H}^{\mathrm{T}} = f(\mathbf{W}^1\mathbf{X} + \mathbf{B}^1) = [h_1, h_2, \ldots, h_{n_H}]^{\mathrm{T}}, \quad h_i = f\left(\sum_{j=1}^{n_I} w_{i,j}^1 x_j + b_i^1\right), \tag{C3}$$

where f denotes the activation function to carry out the nonlinear mapping of the FNN, and the superscript "T" denotes the transpose of matrix. After the data transmission of multiple hidden layers, the matrices of weight and bias coefficient connecting the last hidden layer and the output layer are

$$\mathbf{W}^{L+1} = \begin{bmatrix} w_{1,1}^{L+1} & w_{1,2}^{L+1} & \cdots & w_{1,n_H}^{L+1} \\ w_{2,1}^{L+1} & w_{2,2}^{L+1} & \cdots & w_{2,n_H}^{L+1} \\ \vdots & \vdots & \ddots & \vdots \\ w_{n_O,1}^{L+1} & w_{n_O,2}^{L+1} & \cdots & w_{n_O,n_H}^{L+1} \end{bmatrix}, \quad \mathbf{B}^{L+1} = [b_1^L, b_2^{L+1}, \ldots, b_{n_O}^{L+1}], \tag{C4}$$

where $w_{ij}^{L+1}(i = 1, 2, \ldots, n_O; j = 1, 2, \ldots, n_H)$ denotes the weight coefficient connecting the ith neuron in the output layer and the jth neuron in the Lth hidden layer, b_i^{L+1} denotes the bias coefficient for the ith neuron in the output layer, and n_O is the number of neurons in the output layer.

The output of the FNN is calculated by

$$\mathbf{Y}^* = \mathbf{W}^{L+1}\mathbf{H}^{\mathrm{T}} + \mathbf{B}^{L+1} = [y_1^*, y_2^*, \ldots, y_{n_o}^*], \quad y_i^* = \sum_{j=1}^{n_H} w_{ij}^{L+1} h_j + b_i^{L+1}. \tag{C5}$$

APPENDIX D: THE CELL-INTEGRATED FORM OF THE WW WALL MODEL

In this Appendix, the employed WW model is described. In the WW model, the wall shear stress is computed based on the linear profile and the power law for the viscous sublayer and above, respectively, as follows:

$$u^+ = \begin{cases} y^+, & y^+ \leqslant y_C^+, \\ A(y^+)^B, & y^+ > y_C^+, \end{cases} \tag{D1}$$

where $A = 8.3$, $b = 1/7$, $y_C^+ = A^{1/(1-B)}$, $u^+ = u/u_\tau$, and $y^+ = y u_\tau/\nu$. The velocity varies significantly in the first off-wall grid cell, i.e., the law of the wall changing from the one for the viscous sublayer to that for the logarithmic region. This means that the velocity of the first-wall grid cell can be treated differently. One way is to consider the velocity at the center of the first off-wall cell as the velocity at the cell center location, i.e., the pointwise approach; the other way is to treat it as the mean averaged over the cell (i.e., the cell-integrated form) as follows:

$$\frac{U_p}{u_\tau} = \frac{1}{\Delta y^+} \int_0^{\Delta y^+} u^+(y^+) dy^+, \tag{D2}$$

where U_p denotes the velocity at the center of the first off-wall cell, and $\Delta y^+ = \Delta y u_\tau/\nu$ denotes the wall-normal grid size in wall unit. Substituting Eq. (D1) into Eq. (D2), the expression for the wall shear stress is obtained as follows:

$$|\tau_w| = \begin{cases} \rho \frac{2\nu|U_p|}{\Delta y}, & |U_p| \leqslant \frac{\nu}{2\Delta y} A^{\frac{2}{1-B}}, \\ \rho\left[\frac{1-B}{2} A^{\frac{1+B}{1-B}} \left(\frac{\nu}{\Delta y}\right)^{1+B} + \frac{1+B}{A} \left(\frac{\nu}{\Delta y}\right)^B |U_p|\right]^{\frac{2}{1+B}}, & |U_p| > \frac{\nu}{2\Delta y} A^{\frac{2}{1-B}}. \end{cases} \tag{D3}$$

The cell-integrated form of the WW model shown in Eq. (D3), which was shown to have a better performance than the pointwise approach [43], is employed in this work.

[1] P. Moin and K. Mahesh, Direct numerical simulation: A tool in turbulence research, Annu. Rev. Fluid Mech. **30**, 539 (1998).

[2] H. Choi and P. Moin, Grid-point requirements for large eddy simulation: Chapman's estimates revisited, Phys. Fluids **24**, 011702 (2012).

[3] G. W. He, G. D. Jin, and Y. Yang, Space-time correlations and dynamic coupling in turbulent flows, Annu. Rev. Fluid Mech. **49**, 51 (2017).

[4] U. Piomelli and E. Balaras, Wall-layer models for large-eddy simulations, Annu. Rev. Fluid Mech. **34**, 349 (2002).

[5] W. Cabot and P. Moin, Approximate wall boundary conditions in the large-eddy simulation of high Reynolds number flow, Flow Turbul. Combust. **63**, 269 (2000).

[6] L. Davidson, Large eddy simulations: How to evaluate resolution, Int. J. Heat Fluid Flow **30**, 1016 (2009).

[7] U. Piomelli, Wall-layer models for large-eddy simulations, Prog. Aerosp. Sci. **44**, 437 (2008).

[8] S. T. Bose and G. I. Park, Wall-modeled large-eddy simulation for complex turbulent flows, Annu. Rev. Fluid Mech. **50**, 535 (2018).

[9] K. Duraisamy, G. Iaccarino, and H. Xiao, Turbulence modeling in the age of data, Annu. Rev. Fluid Mech. **51**, 357 (2019).

[10] S. L. Brunton, B. R. Noack, and P. Koumoutsakos, Machine learning for fluid mechanics, Annu. Rev. Fluid Mech. **52**, 477 (2020).

[11] S. B. Pope, *Turbulent Flows* (Cambridge University Press, Cambridge, UK, 2000).

[12] M. Wang and P. Moin, Dynamic wall modeling for large-eddy simulation of complex turbulent flows, Phys. Fluids **14**, 2043 (2002).

[13] S. Kawai and J. Larsson, Dynamic non-equilibrium wall-modeling for large eddy simulation at high Reynolds numbers, Phys. Fluids **25**, 015105 (2013).

[14] G. I. Park and P. Moin, An improved dynamic non-equilibrium wall-model for large eddy simulation, Phys. Fluids **26**, 015108 (2014).

[15] G. I. Park, Wall-modeled large-eddy simulation of a high Reynolds number separating and reattaching flow, AIAA J. **55**, 3709 (2017).

[16] X. I. A. Yang, J. Sadique, R. Mittal, and C. Meneveau, Integral wall model for large eddy simulations of wall-bounded turbulent flows, Phys. Fluids **27**, 025112 (2015).

[17] A. Lozano-Durán, M. G. Giometto, G. I. Park, and P. Moin, Non-equilibrium three-dimensional boundary layers at moderate Reynolds numbers, J. Fluid Mech. **883**, A20 (2020).

[18] S. Kawai and J. Larsson, Wall-modeling in large eddy simulation: Length scales, grid resolution, and accuracy, Phys. Fluids **24**, 015105 (2012).

[19] D. Chung and D. I. Pullin, Large-eddy simulation and wall modelling of turbulent channel flow, J. Fluid Mech. **631**, 281 (2009).

[20] W. Cheng, D. I. Pullin, and R. Samtaney, Large-eddy simulation of separation and reattachment of a flat plate turbulent boundary layer, J. Fluid Mech. **785**, 78 (2015).

[21] S. T. Bose and P. Moin, A dynamic slip boundary condition for wall-modeled large-eddy simulation, Phys. Fluids **26**, 015104 (2014).

[22] H. J. Bae, A. Lozano-Durán, S. T. Bose, and P. Moin, Turbulence intensities in large-eddy simulation of wall-bounded flows, Phys. Rev. Fluids **3**, 014610 (2018).

[23] J. Larsson, S. Kawai, J. Bodart, and I. Bermejo-Moreno, Large eddy simulation with modeled wall-stress: Recent progress and future directions, Mech. Engin. Rev. **3**, 15 (2016).

[24] A. Frere, K. Hillewaert, L. P. Chatelain, and G. Winckelmans, High Reynolds number airfoil: From wall-resolved to wall-modeled LES, Flow Turbul. Combust. **101**, 457 (2018).

[25] H. J. Bae, A. Lozano-Durán, S. T. Bose, and P. Moin, Dynamic slip wall model for large-eddy simulation, J. Fluid Mech. **859**, 400 (2019).

[26] J. Ling, A. Kurzawski, and J. Templeton, Reynolds averaged turbulence modelling using deep neural networks with embedded invariance, J. Fluid Mech. **807**, 155 (2016).

[27] Z. D. Zhou, G. W. He, S. Z. Wang, and G. D. Jin, Subgrid-scale model for large-eddy simulation of isotropic turbulent flows using an artificial neural network, Comput. Fluids **195**, 104319 (2019).

[28] R. King, O. Hennigh, A. Mohan, and M. Chertkov, From deep to physics-informed learning of turbulence: Diagnostics, arXiv:1810.07785v2.

[29] S. Lee and D. You, Data-driven prediction of unsteady flow over a circular cylinder using deep learning, J. Fluid Mech. **879**, 217 (2019).

[30] K. Fukami, K. Fukagata, and K. Taira, Super-resolution reconstruction of turbulent flows with machine learning, J. Fluid Mech. **870**, 106 (2019).

[31] B. Liu, J. P. Tang, H. B. Huang, and X. Y. Lu, Deep learning methods for super-resolution reconstruction of turbulent flows, Phys. Fluids **32**, 025105 (2020).

[32] J. Ling, R. Jones, and J. Templeton, Machine learning strategies for systems with invariance properties, J. Comput. Phys. **318**, 22 (2016).

[33] J.-X. Wang, J.-L. Wu, and H. Xiao, Physics-informed machine learning approach for reconstructing Reynolds stress modeling discrepancies based on DNS data, Phys. Rev. Fluids **2**, 034603 (2017).

[34] J.-L. Wu, H. Xiao, and E. Paterson, Physics-informed machine learning approach for augmenting turbulence models: A comprehensive framework, Phys. Rev. Fluids **3**, 074602 (2018).

[35] M. Gamahara and Y. Hattori, Searching for turbulence models by artificial neural network, Phys. Rev. Fluids **2**, 054604 (2017).

[36] R. Maulik, O. San, A. Rasheed, and P. Vedula, Data-driven deconvolution for large eddy simulations of Kraichnan turbulence, Phys. Fluids **30**, 125109 (2018).

[37] A. Vollant, G. Balarac, and C. Corre, Subgrid-scale scalar flux modelling based on optimal estimation theory and machine-learning procedures, J. Turbul. **18**, 854 (2017).

[38] M. Milano and P. Koumoutsakos, Neural network modeling for near wall turbulent flow, J. Comput. Phys. **182**, 1 (2002).

[39] X. I. A. Yang, S. Zafar, J.-X. Wang, and H. Xiao, Predictive large-eddy-simulation wall modeling via physics-informed neural networks, Phys. Rev. Fluids **4**, 034602 (2019).

[40] X. L. D. Huang, X. I. A. Yang, and R. F. Kunz, Wall-modeled large-eddy simulations of spanwise rotating turbulent channels: Comparing a physics-based approach and a data-based approach, Phys. Fluids **31**, 125105 (2019).

[41] A. Lozano-Durán and H. J. Bae, Self-critical machine-learning wall-modeled LES for external aerodynamics, arXiv:2012.10005v1.

[42] J. Fröhlich, C. P. Mellen, W. Rodi, L. Temmerman, and M. A. Leschziner, Highly resolved large-eddy simulation of separated flow in a channel with streamwise periodic constrictions, J. Fluid Mech. **526**, 19 (2005).

[43] L. Temmerman, M. A. Leschziner, C. P. Mellen, and J. Fröhlich, Investigation of wall-function approximations and subgrid-scale models in large eddy simulation of separated flow in a channel with streamwise periodic constrictions, Int. J. Heat Fluid Flow **24**, 157 (2003).

[44] M. Manhart, N. Peller, and C. Brun, Near-wall scaling for turbulent boundary layers with adverse pressure gradient, Theor. Comput. Fluid Dyn. **22**, 243 (2008).

[45] C. Duprat, G. Balarac, O. Métais, P. M. Congedo, and O. Brugière, A wall-layer model for large-eddy simulations of turbulent flows with/out pressure gradient, Phys. Fluids **23**, 015101 (2011).

[46] M. Breuer, N. Peller, C. Rapp, and M. Manhart, Flow over periodic hills: Numerical and experimental study in a wide range of Reynolds numbers, Comput. Fluids **38**, 433 (2009).

[47] C. Rapp and M. Manhart, Flow over periodic hills: An experimental study, Exp. Fluids **51**, 247 (2011).

[48] B. Krank, M. Kronbichler, and W. A. Wall, Direct numerical simulation of flow over periodic hills up to Re_h=10 595, Flow Turbul. Combust. **101**, 521 (2018).

[49] H. Xiao, J.-L. Wu, S. Laizet, and L. Duan, Flows over periodic hills of parameterized geometries: A dataset for data-driven turbulence modeling from direct simulations, Comput. Fluids **200**, 104431 (2020).

[50] X. L. Yang, F. Sotiropoulos, R. J. Conzemius, J. N. Wachtler, and M. B. Strong, Large-eddy simulation of turbulent flow past wind turbines/farms: The Virtual Wind Simulator (VWiS), Wind Energy **18**, 2025 (2015).

[51] X. L. Yang and F. Sotiropoulos, A new class of actuator surface models for wind turbines, Wind Energy **21**, 285 (2018).

[52] S. Kang and F. Sotiropoulos, Numerical modeling of 3D turbulent free surface flow in natural waterways, Adv. Water Resour. **40**, 23 (2012).

[53] S. Kang, X. L. Yang, and F. Sotiropoulos, On the onset of wake meandering for an axial flow turbine in a turbulent open channel flow, J. Fluid Mech. **744**, 376 (2014).

[54] A. Khosronejad and F. Sotiropoulos, Numerical simulation of sand waves in a turbulent open channel flow, J. Fluid Mech. **753**, 150 (2014).

[55] X. L. Yang, A. Khosronejad, and F. Sotiropoulos, Large-eddy simulation of a hydrokinetic turbine mounted on an erodible bed, Renew. Energy **113**, 1419 (2017).

[56] X. L. Yang and F. Sotiropoulos, On the dispersion of contaminants released far upwind of a cubical building for different turbulent inflows, Build. Environ. **154**, 324 (2019).

[57] X. L. Yang and F. Sotiropoulos, Wake characteristics of a utility-scale wind turbine under coherent inflow structures and different operating conditions, Phys. Rev. Fluids **4**, 024604 (2019).

[58] D. Foti, X. L. Yang, L. Shen, and F. Sotiropoulos, Effect of wind turbine nacelle on turbine wake dynamics in large wind farms, J. Fluid Mech. **869**, 1 (2019).

[59] A. Khosronejad, K. Flora, and S. Kang, Effect of inlet turbulent boundary conditions on scour predictions of coupled LES and morphodynamics in a field-scale river: Bankfull flow conditions, J. Hydraul. Eng. **146**, 04020020 (2020).

[60] M. Germano, U. Piomelli, P. Moin, and W. H. Cabot, A dynamic subgrid-scale eddy viscosity model, Phys. Fluids A **3**, 1760 (1991).

[61] L. Ge and F. Sotiropoulos, A numerical method for solving the 3D unsteady incompressible Navier-Stokes equations in curvilinear domains with complex immersed boundaries, J. Comput. Phys. **225**, 1782 (2007).

[62] S. Kang, A. Lightbody, C. Hill, and F. Sotiropoulos, High-resolution numerical simulation of turbulence in natural waterways, Adv. Water Resour. **34**, 98 (2011).

[63] X. I. A. Yang, G. I. Park, and P. Moin, Log-layer mismatch and modeling of the fluctuating wall stress in wall-modeled large-eddy simulations, Phys. Rev. Fluids **2**, 104601 (2017).

[64] X. I. A. Yang, S. Bose, and P. Moin, A physics-based interpretation of the slip-wall LES model, Center for Turbulence Research (Annual Research Briefs 2016) (Stanford University, Stanford, CA, 2017), pp. 65–74, https://web.stanford.edu/group/ctr/ResBriefs/2016/Reports/006_Xiang_1.pdf.

[65] I. Goodfellow, Y. Bengio, and A. Courville, *Deep Learning* (MIT Press, Cambridge, MA, 2016).

[66] D. P. Kingma and J. Ba, Adam: A method for stochastic optimization, arXiv:1412.6980v9.

[67] H. Werner and H. Wengle, Large-eddy simulation of turbulent flow over and around a cube in a plate channel, in *Eighth Symposium on Turbulent Shear Flows* (Springer, Berlin, 1993).

[68] Johns Hopkins turbulence database, http://turbulence.pha.jhu.edu.

[69] M. Lee and R. D. Moser, Direct numerical simulation of turbulent channel flow up to $Re_\tau \approx 5200$, J. Fluid Mech. **774**, 395 (2015).

[70] G. P. Almeida, D. F. G. Durão, and M. V. Heitor, Wake flows behind two-dimensional model hills, Exp. Therm. Fluid Sci. **7**, 87 (1993).